Vibrational coherences in manganese single-molecule magnets after ultrafast photoexcitation

Vibrational coherences in manganese single-molecule magnets after ultrafast photoexcitation

Florian Liedy[1], Julien Eng[2], Robbie McNab[1], Ross Inglis[1], Thomas J. Penfold[2], Euan K. Brechin[1], J. Olof Johansson[1,*]

[1]*EaStCHEM School of Chemistry, University of Edinburgh, David Brewster Road, EH9 3FJ, Edinburgh, UK*

[2] *Chemistry - School of Natural and Environmental Sciences, Newcastle University, Newcastle upon Tyne, NE1 7RU, UK*

**Email: olof.johansson@ed.ac.uk*

Abstract

Magnetic recording using femtosecond laser pulses has recently been achieved in some dielectric media, showing potential for ultrafast data-storage applications. Single-Molecule Magnets (SMMs) are metal complexes with two degenerate magnetic ground states and are promising for increasing storage density but remain unexplored using ultrafast techniques. Here, we have explored the dynamics occurring after photoexcitation of a trinuclear μ_3-oxo-bridged Mn(III)-based SMM, whose magnetic anisotropy is closely related to the Jahn-Teller distortion. Ultrafast transient absorption spectroscopy in solution reveals oscillations superimposed on the decay traces due to a vibrational wavepacket. Based on complementary measurements and calculations on the monomer $Mn(acac)_3$, we conclude that the wavepacket motion in the trinuclear SMM is constrained along the Jahn-Teller axis due to the μ_3-oxo and μ-oxime bridges. Our results provide new possibilities for optical control of the magnetisation in SMMs on femtosecond timescales and open up new molecular-design challenges to control the wavepacket motion in the excited state of polynuclear transition-metal complexes.

Single-Molecule Magnets (SMMs), i.e. molecules that show magnetic hysteresis below a certain blocking temperature[1], hold great promise for future applications in data storage devices[2] because their small size and well-defined magnetic properties can reduce the size of data bits and therefore increase storage density. Being able to switch the magnetisation direction in SMMs using femtosecond laser pulses could provide the technology for future ultradense memory devices operating on unprecedented timescales[3]. So far the most promising process of ultrafast optical spin switching in inorganic molecules has been intersystem crossing (ISC) from low-spin $S = 0$ to high-spin $S = 2$ in Fe(II) complexes, taking place in less than 200 fs[4–7]. The sudden change in electronic structure upon photoexcitation, launches a vibrational wavepacket along the Fe–N bonds, mainly involving the breathing mode around 126 cm^{-1} [5,6,8], which can be observed using transient absorption (TA) spectroscopy. The work on Fe(II) and the observation of sub-200 fs ISC in $Cr(acac)_3$[9,10], have provided an excellent basis for understanding how fast spins can be manipulated in transition metal complexes. However, for magnetic applications one also needs to consider the magnetic anisotropy in addition to spin switching dynamics. Magnetic anisotropy, which is important for SMM behaviour, is ubiquitous in magnetic data storage devices because it gives the magnetisation a preferred direction. Despite the potential of photo-switching in SMMs, there are a limited number of studies of ultrafast dynamics in molecule-based magnets. For example, ultrafast charge-transfer dynamics[11], phase-transitions[12] and ISC[13] have been studied in magnetic Prussian blue analogues, and spin state switching has been observed in Cu(II)-based breathing crystals[14]. Magnetic nanotoruses have been studied using TA spectroscopy, identifying lanthanides as trap states for excitons[15].

Manganese-based coordination complexes, such as Mn_{12}[16,17], have been instrumental in the development of SMMs and are typically magnetically bistable due to a large, negative zero-field splitting caused by the magnetic anisotropy of individual Mn(III) ions. The anisotropy in the Mn(III) ion arises because of the electronic configuration $t_{2g}^3 e_g^1$ leads to a Jahn-Teller (JT) distortion. Together with the spin-orbit interaction, this anisotropy in Mn(III)-based SMMs leads

to two degenerate magnetic ground states, where the ground state spin is saturated either parallel or anti-parallel to the magnetic easy axis. Transiently reducing the anisotropy in SMMs, using femtosecond laser pulses, could provide a method towards achieving optical control of their magnetisation direction. The prototype Mn-based SMM $Mn_{12}Ac$ (Ac = acetate) is promising for exploring optical modulation of the anisotropy because it has been shown that reorienting the JT axis with high pressure can strongly influence its magnetic properties[18]. Similarly, there have been reports of ultrafast spin-switching of Cu(II) molecule-based magnets due to optical modulation of the JT axis[14,19]. However, said species are large and structurally complex, with smaller molecules being better suited to achieving a more detailed understanding of the photophysics. One such example is a family of oxime-based SMMs containing three Mn(III) ions whose magneto-structural relationship has been extensively investigated[20,21].

Herein, we present ultrafast transient absorption spectroscopy of the SMM $[Mn(III)_3O(Et\text{-}sao)_3(\beta\text{-}pic)_3(ClO_4)]$, or "$Mn_3$", which has three Mn(III) ions arranged in a triangle[20], where the ions are connected via a μ_3-oxo bridge and peripheral –N–O– (oxime) bonds and display a JT distortion perpendicular to the plane of the triangle (Figure 1**a**). Ferromagnetic interactions between the three S = 2 ions results in an S = 6 ground state. Even though the Mn_3 is a relatively small SMM, it still provides a formidable challenge for theory because of the large spin ground state. We have therefore also studied the Mn(III) monomer $Mn(acac)_3$, which is not an SMM but serves as a model system for a simpler JT-distorted Mn(III) ion[22] (Figure 1**a**). Our experimental and computational results show that photoexcitation of the Mn(III) complexes leads to a coherent vibrational wavepacket in the lowest excited state (Figure 1**c**), which corresponds to a switch from axial to equatorial JT distortion by compressing the axial bonds and elongating the equatorial bonds. In Mn_3, the strong equatorial bonds due to the μ_3-oxo and μ–oxime bridges, prevents a JT switch, which leads to a collective motion of the Mn ions along the weaker axial JT bonds. These measurements open up the possibility to explore the anisotropy in SMMs via wavepackets on the femtosecond timescale.

Results

Mononuclear $Mn(acac)_3$

The absorption spectrum of $Mn(acac)_3$ in ethanol is shown in Figure 2**a**, where the three expected metal-centred (MC) transitions for a Mn(III) complex can be seen at 800, 600 and 400 nm, in agreement with previous work[23,24]. In the transient absorption experiment, the pump wavelength was set to λ = 400 nm, which multi-configurational calculations at the CASSCF//NEVPT2 level (Figure 2**b**-**e** and Supplementary Tab. 3) identify as predominantly the d_{xz}/d_{yz} to $d_{x^2-y^2}$ transition (^5E_g) (Figure 2**d**), but with some overlap with ligand-centred transitions (Figure 2**e**).

TA spectra of $Mn(acac)_3$ in ethanol after exciting at 400 nm are presented in Figure 3**a**, where the difference spectra for selected time delays are shown. During the first picosecond, two positive bands due to excited-state absorption (ESA) were observed around 360 ("UV-band") and 430 nm ("Vis-band"). The maxima of both the UV- and Vis-bands are shifted towards shorter wavelengths for longer time delays for both molecules. The Vis band decays with an initially fast component over the first few ps, and eventually reaches a plateau and stays the same for the maximum delay measured (200 ps). The Glotaran software[25] was used for a sequential global analysis. For $Mn(acac)_3$, four exponential decays were needed to obtain a good fit, with corresponding pre-exponential factors A_x and time constants τ_x (x = 1 − 4). A fast decay constant of τ_1 = 250 ± 30 fs and two intermediate time constants τ_2 = 1.0 ± 0.2 ps and τ_3 = 5.2 ± 0.5 ps were found. To account for the observed plateau, a longer time constant of τ_4 = 400 ps was included in the fit. The decay-associated spectra (DAS), corresponding to the spectral dependence of A_x, for $Mn(acac)_3$ are shown in Figure 3**b**.

Oscillations were observed in the kinetic trace of the Vis band for $Mn(acac)_3$, which is shown in Figure 4**a** (further kinetic traces can be found in Supplementary Figures 5-6). The oscillations are more clearly seen in Figure 4**c**, where the fits from the global analysis have been subtracted and damped cosine functions have been fitted to the data. For $Mn(acac)_3$, we

found that the oscillations could be reasonably described by two frequencies, namely 170 ± 5 and 208 ± 6 cm^{-1}. The oscillations decayed with a $\tau_{osc}^{Mn(acac)_3} = 325 \pm 11$ fs time constant. A Fourier analysis of the fit residues is shown in Figure 5**a**, where two peaks at $\tilde{v}_1^{Mn(acac)_3} = 167$ and $\tilde{v}_2^{Mn(acac)_3} = 215\ cm^{-1}$ on top of a broader band can be observed. Since oscillations like these are a signature of a fast motion out of the Franck-Condon region via a vibrational wavepacket comprised of vibrational modes of the molecule in either the ground or excited state[5], we have performed Raman spectroscopy on crystal grains of the molecular solids to compare the vibrational spectra to the oscillations observed in the transient absorption. We cannot determine the vibrational spectrum in the excited state but the ground-state Raman spectrum provides a good starting point. The resulting spectra are shown in Figure 5**a** for $Mn(acac)_3$.

Trinuclear Mn_3

The static UV/Vis absorption spectrum of Mn_3, shown in Figure 2**a**, also displayed similar absorption bands in the visible region as $Mn(acac)_3$, although with an order of magnitude larger extinction coefficients. We have not been able to perform multi-configurational calculations of Mn_3 due to the large number of unpaired electrons. The TA results for Mn_3 were largely similar to $Mn(acac)_3$ and both the UV and Vis bands were observed, as seen in Figure 3**c**. The global analysis yielded three time constants, a fast decay constant of τ_1 = 180 ± 10 fs, an intermediate τ_2 = 1.8 ± 0.2 ps and finally a longer time constants τ_3 = 9 ± 1 ps, which importantly is shorter than what was observed for $Mn(acac)_3$. Oscillations were also observed for Mn_3, as seen in Figure 4**b**. However, the oscillations could be described with only one frequency component of 181 ± 3 cm^{-1}, in agreement with the $\tilde{v}_1^{Mn_3} = 185\ cm^{-1}$ peak in the Fourier transform (Figure 5**b**). The oscillation decay time was $\tau_{osc}^{Mn_3} = 360 \pm 15$ fs.

TA measurements on both $Mn(acac)_3$ and Mn_3 exciting at 535 nm were also performed, yielding similar results to 400 nm excitation. For these measurements, a high concentration was needed because of the low extinction coefficient at the pump wavelength, and for

Mn(acac)$_3$ the UV band was therefore not observed. These data are presented in Supplementary Figure 7.

Discussion

We first discuss the results of Mn(acac)$_3$ because the multi-configurational calculations have allowed us to assign the absorption spectrum and identify the lowest excited MC state. From the transient absorption data for Mn(acac)$_3$, we extract four time-constants in a sequential decay model. The A_2 and A_3 DAS (and to some extent A_4) are different to A_1, which implies that there is a change in the electronic character of the excited state[9] on a <300 fs timescale via internal conversion (IC). The 0.15 ps TA spectrum in Figure 3**b** therefore corresponds to the absorption from the initially excited state, which absorbs predominantly in the visible spectral region. Because the Mn(acac)$_3$ TA spectra do not change from a few ps to >200 ps, we can assume that the lowest excited state is populated ($^5A_{1g}$, Figure 1**c**). The UV band predominantly decays with the τ_2 = 1.0 and τ_3 = 5.2 ps time constants and is not observed in the A_4 DAS, where a slight negative signal can be seen instead. If the UV and Vis bands corresponded to two different species, the UV band would be replaced with a GSB for times longer than 10-20ps, which is not the case. It therefore appears the UV ESA oscillator strength is overtaken by the GSB during the structural dynamics/vibrational cooling taking place as the molecule adjusts to the lowest excited state geometry, which is also manifested in the anisotropy data shown in Supplementary Figure 8. As previously mentioned, we have excited at both 400 ($^5B_{1g} \rightarrow {}^5E_g$) and 535 nm ($^5B_{1g} \rightarrow {}^5B_{2g}$, which does not show any charge-transfer character because $\varepsilon(535\ nm) = 93\ L\ mol^{-1}cm^{-1}$) and found the same TA spectrum after the first few 100 fs. This supports the interpretation that the lowest MC state has become populated. This observation is similar to what has been observed in Cr(acac)$_3$[9] and Fe(acac)$_3$[26]. The main difference is that in both these molecules, the lowest excited state corresponds to a change in spin state via ISC because of the d^3 and d^5 electron configurations. However, in Mn(acac)$_3$, there is no change in spin multiplicity and the electronic process is IC instead of ISC. Since the $^5A_{1g}$ excited state corresponds to promoting an electron from the d_{z^2}

orbital to the $d_{x^2-y^2}$ orbital, the Mn–O bond along the z-axis is shortened whereas the equatorial bonds are elongated leading to a shift in the JT distortion from axial to equatorial. Once in the $^5A_{1g}$ state, the 1.0 and 5.2 ps decay constants can be assigned to vibrational cooling via intramolecular vibrational redistribution (IVR) and energy dissipation to the solvent. The vibrational cooling can be inferred from the spectral narrowing and blue-shift in the absorption peak[9], as observed in Figure 3**a**. The two ps-timescales are not necessarily a reflection of population dynamics (because of difficulties fitting spectral narrowing and blue-shifts) but should be taken as a measure of the characteristic timescales for reaching the minimum on the excited state potential.

Identifying the reaction coordinate for the wavepacket could provide further information about the excited state. The wavenumbers of the Fourier transform of the wavepacket coincides with the observed Raman modes around 200 cm^{-1}, as seen in Figure 5**a**. The wavepacket survives the IC, but this, together with vibrational cooling and IVR, leads to the observed dephasing of the wavepacket (325 ± 11 fs). $Mn(acac)_3$ is flexible enough to adjust for the JT-shifted state, which is why the $^5A_{1g}$ state has such long lifetime. The structural change from the $^5B_{1g}$ to $^5A_{1g}$ states can be associated with many vibrational modes in the 200 cm^{-1} region and therefore no one normal mode can be described as the reaction coordinate. The photophysical model for $Mn(acac)_3$ is summarised in Figure 6.

Given the complexity of even $Mn(acac)_3$, it is difficult to assign the specific transitions responsible for the ESA spectrum. There are several quintet transitions from the $^5A_{1g}$ state identified in the calculations (Supplementary Tab. 4), where ^{5}MC transitions are observed around 470-530 nm and ligand-centred transitions at 310-333 nm. Red-shifted metal-to-ligand charge-transfer (MLCT) transitions could also contribute to the UV band. Nevertheless, a definitive assignment of the ESA is outside the scope of this work and we emphasise that the important result from the $Mn(acac)_3$ study is the population of the JT-switched $^5A_{1g}$ state.

We will now interpret the results of Mn_3 in light of the findings for $Mn(acac)_3$. The electronic structure of Mn_3 is determined by the μ_3-oxo and μ-oxime bridges connecting the three Mn(III)

ions together, which with the number of unpaired electrons and the exchange coupling between them, lead to a large array of spin states. Given the similarity to $Mn(acac)_3$ and the observation of the three characteristic Mn(III) peaks in the visible spectrum, we assign the visible absorption to transitions between different *d* electronic bands.

The TA results of Mn_3 are also similar to $Mn(acac)_3$. As with $Mn(acac)_3$, we assign τ_1 = 180 fs to the electronic decay into the $d_{x^2-y^2}$ band. Due to the large spin ground state, it is difficult to conclude anything about different spin projections or if the relaxation process proceeds via IC or ISC. The τ_2 = 1.9 ps time constant can be assigned to vibrational cooling in the $d_{x^2-y^2}$ manifold. The most significant difference between $Mn(acac)_3$ and Mn_3 was that we did not observe any long-lived component, and the shortest decay was τ_3 = 9 ps. A transition into the $d_{x^2-y^2}$ orbital manifold will induce a change in the charge distribution in the molecule, which will affect the JT distortion, as was the case for $Mn(acac)_3$ and which has been observed in perovskite manganites[27]. We interpret these observations such that the UV and Vis bands are signatures of the shift towards a JT switched state, but because of the strong bonds in the triangle, due to the μ_3-oxo and μ-oxime bridges, the molecule cannot relax to the geometrical equilibrium of the excited state required for switching from axial to equatorial JT distortion. In this case, the molecule relaxes back to the electronic ground state corresponding to an axial JT distortion with a 9 ps time constant.

The oscillations of the wavepacket in Mn_3 can be described by a single frequency component 185 cm^{-1} (Figure 5**b**). The Raman peak at 213 cm^{-1} is in good agreement with the calculated mode at 210 cm^{-1}, which can be described as a collective in-phase asymmetric stretch-mode along the JT axis for all three Mn ions (Supplementary Video 1), where the Mn–O bonds are contracted while the Mn–N bonds are extended and there is a flattening of the Mn triangle. The reason we observe the wavepacket more clearly in Mn_3 (Figure 4), is because the strong equatorial bonds restrict the expansion in the plane and so the main reaction coordinate for the wavepacket is along the axial JT distortion, which results in a simpler reaction coordinate. The inability for Mn_3 to expand equatorially significantly reduces the lifetime of the excited

state to τ_3 = 9 ps for Mn_3 versus τ_4 > 200 ps for $Mn(acac)_3$. The wavepacket is most likely associated with the excited state since the oscillations are observed in the Vis band (ESA), where there is little contribution from any GSB. Furthermore, the wavepacket frequency is lower in energy than the ground state Raman peak due to the weaker bonds in the excited state. Also, the oscillations are cosine-like, implying a displacive character of the wavepacket generation mechanism. Because of these reasons, a contribution from ground-state coherence is therefore not likely. We have carried out anisotropy measurements on both $Mn(acac)_3$ and Mn_3 (Supplementary Fig. 8). However, since MC transitions typically give rise to little anisotropy[28,29], which is what we also observe, the measurements did not give any new information on the change in JT distortion.

We finish by mentioning that we have also carried out measurement of the more complex $[Mn(III)_6O_2(Et\text{-}sao)_6(O_2CPh(Me)_2)_2(EtOH)_6]$, or "$Mn_6$", which contains six high-spin Mn(III) ions arranged in two triangles[30] and the results are presented in Supplementary Figures 10-12. In Mn_6, all Mn(III) ions are ferromagnetically coupled and the ground state is S = 12. The results were similar to Mn_3 and we even observe oscillations in the kinetic traces. The wavepacket contains several modes but the complex nature of this molecule and the large density of states, preclude a more detailed analysis.

In summary, we have performed transient absorption spectroscopy of the axial Jahn-Teller (JT) distorted Mn(III) monomer $Mn(acac)_3$ and the trinuclear single-molecule magnet Mn_3 in ethanol at room temperature. Multiconfigurational calculations show that the excited state corresponds to a shift from axial to equatorial JT distortion. Oscillations superimposed on the decay signals were attributed to a vibrational wavepacket formed as the molecule adjusts to the new JT distortion. In Mn_3, the strong equatorial bonds involving the μ_3-oxo and μ-oxime bridges, prevent the shift from axial to equatorial JT compression and force the wavepacket motion predominantly along the JT axis, resulting in a simpler reaction coordinate and longer dephasing time. These observations open up design strategies for achieving ultrafast coherences in complex chemical systems for control and function-enhancement, which are

actively being developed[31]. There have recently been several interesting observations in metal complexes, such as retention of vibrational coherence during intersystem crossing in $Cr(acac)_3$[10], metal-metal bond modulations in di-Pt(II) complexes[32] and in particular it has been shown that JT distortions, such as in Cu(I) complexes[33], are important. Our work contributes to this field by demonstrating vibrational coherences in a molecule with as many as six metal ions. Furthermore, there is a peak in the Raman spectrum of the $Mn_{12}Ac$[34] SMM at 209 cm^{-1} and so it is possible that our approach is more general, which is supported by the observation of light-induced magnetisation changes in another Mn_{12} complex using continuous irradiation[35].

Methods

Materials

The synthesis of the complexes has been described previously in Ref.[36] for Mn_6 and in Ref.[20] for Mn_3. $Mn(acac)_3$ was bought from Sigma-Aldrich and used without further purification. For the transient absorption measurement, the complexes were dissolved in ethanol. The concentrations were 14.8, 1.88, and 1.8 mmol/l for $Mn(acac)_3$, Mn_3, and Mn_6, respectively. A Starna flow cuvette with 0.2 mm pathlength was used for the TA measurements with a flow of 8 µl/min.

Optical measurements

The TA setup is based on the apparatus described in ref.[37]. As the pump beam, the second harmonic (400 nm) of a Coherent Legend Elite laser was used (pulse duration 120 fs and output 800 nm wavelength). The pump pulses were focused into the sample by a f = −500 mm concave mirror producing a spot size of 226 microns ($1/e^2$). The laser fluence was 3.3 mJ/cm^2. For the probe and reference beams 1.4 µJ/pulse of the 800 nm fundamental was focused with an f = 100 mm fused silica lens in a 5 mm thick CaF_2 plate, which was continuously moved in two dimensions, to produce a broadband white light continuum. The white light was collimated with an f = −100 mm concave mirror and the 800 nm fundamental was removed with a 720 nm

cut off filter. The detected probe spectrum ranged from 320 to 720 nm. The white light beam was divided with a reflective metallic neutral density filter for probe and reference. The probe light was focused into the sample with an f = −500 mm concave mirror. The probe beam diameter in the sample was 105 µm ($1/e^2$). To avoid anisotropic signals, the pump-probe polarization angle was set to 54.7° (“magic angle”).

For controlling the time delay between pump and probe, a delay stage with mounted retroreflector was used. For each time delay 1000 spectra were collected. The whole procedure was repeated five times to get 5000 spectra in total for each delay position. A prism was used to disperse the white-light beams onto two fast CCD cameras from Entwicklungsbuero Stresing equipped with Hamamatsu S7031-0906 sensors with 512x58 active pixels. Full binning was used, where the 58 vertical pixel were binned, which allowed a synchronous read-out at 1 kHz for both probe and reference beams.

Raman spectroscopy of crystal grains of the complexes was performed on a Renishaw Raman microscope with a laser wavelength of 785 nm.

Computations

The details and results of the computations are presented in the Supplementary Section 1.

Data availability

The raw transient absorption data (incl. anisotropy measurements), Raman and UV-Vis spectra, and computational data that support the findings of this study are available in the Edinburgh DataShare repository with the identifier doi:.

Competing interests

The authors declare no competing interests.

Author contributions

FL performed the optical experiments and analysed the data and RMcN synthesized and characterised the samples under the supervision of RI and EKB. JE and TJP carried out the DFT calculations. FL, EKB and JOJ conceived the experiments and interpreted the results. FL and JOJ co-wrote the paper. All authors discussed the results and commented on the manuscript.

Acknowledgements

This work was supported by funding from the Royal Society of Edinburgh and the Carnegie Trust (Collaborative Research Grant). The authors thank M. D. Horbury and V. Stavros for allowing us to carry out preliminary measurements in their lab and assistance with these measurements. FL and JOJ thank A. Gromov for the help with the Raman spectrometer and E. Riedle for helpful advice with building the TA setup. JOJ is a Royal Society of Edinburgh/BP Trust research fellow. EKB thanks the EPSRC for grants EP/P025986/1 and EP/N01331X/1. TJP and JE thank the EPSRC for grants EP/R021503/1 and EP/P012388/1.

Bibliography

1. Christou, G., Gatteschi, D., Hendrickson, D. N. & Sessoli, R. Single-Molecule Magnets. *MRS Bull.* **25**, 66–71 (2000).

2. Bogani, L. & Wernsdorfer, W. Molecular spintronics using single-molecule magnets. *Nat. Mater.* **7**, 179–86 (2008).

3. Stupakiewicz, A., Szerenos, K., Afanasiev, D., Kirilyuk, A. & Kimel, A. V. Ultrafast nonthermal photo-magnetic recording in a transparent medium. *Nature* **542**, 71–74 (2017).

4. Monat, J. E. & McCusker, J. K. Femtosecond excited-state dynamics of an iron(II) polypyridyl solar cell sensitizer model. *J. Am. Chem. Soc.* **122**, 4092–4097 (2000).

5. Auböck, G. & Chergui, M. Sub-50-fs photoinduced spin crossover in $[Fe(bpy)_3]^{2+}$. *Nat.*

Chem. **7**, 629–633 (2015).

6. Lemke, H. T. *et al.* Coherent structural trapping through wave packet dispersion during photoinduced spin state switching. *Nat. Commun.* **8**, 15342 (2017).

7. Zerdane, S. *et al.* Comparison of structural dynamics and coherence of d-d and MLCT light-induced spin state trapping. *Chem. Sci.* **8**, 4978–4986 (2017).

8. Consani, C. *et al.* Vibrational Coherences and Relaxation in the High-Spin State of Aqueous $[Fe^{II}(bpy)_3]^{2+}$. *Angew. Chemie Int. Ed.* **48**, 7184–7187 (2009).

9. Juban, E. A. & McCusker, J. K. Ultrafast dynamics of ^2E state formation in $Cr(acac)_3$. *J. Am. Chem. Soc.* **127**, 6857–6865 (2005).

10. Schrauben, J. N., Dillman, K. L., Beck, W. F. & McCusker, J. K. Vibrational coherence in the excited state dynamics of $Cr(acac)_3$: probing the reaction coordinate for ultrafast intersystem crossing. *Chem. Sci.* **1**, 405 (2010).

11. Kamioka, H., Moritomo, Y., Kosaka, W. & Ohkoshi, S. Dynamics of charge-transfer pairs in the cyano-bridged Co^{2+}-Fe^{3+} transition-metal compound. *Phys. Rev. B* **77**, 180301 (2008).

12. Asahara, A. *et al.* Ultrafast dynamics of reversible photoinduced phase transitions in rubidium manganese hexacyanoferrate investigated by midinfrared CN vibration spectroscopy. *Phys. Rev. B* **86**, 195138 (2012).

13. Johansson, J. O. *et al.* Directly probing spin dynamics in a molecular magnet with femtosecond time-resolution. *Chem. Sci.* **7**, 7061–7067 (2016).

14. Dong, X., Lorenc, M., Tretyakov, E. V., Ovcharenko, V. I. & Fedin, M. V. Light-Induced Spin State Switching in Copper(II)-Nitroxide-Based Molecular Magnet at Room Temperature. *J. Phys. Chem. Lett.* **8**, 5587–5592 (2017).

15. Baniodeh, A. *et al.* Unraveling the Influence of Lanthanide Ions on Intra- and Inter-

Molecular Electronic Processes in $Fe_{10}Ln_{10}$ Nano-Toruses. *Adv. Funct. Mater.* **24**, 6280–6290 (2014).

16. Caneschi, A. *et al.* Alternating current susceptibility, high field magnetization, and millimeter band EPR evidence for a ground S = 10 state in $[Mn_{12}O_{12}(Ch_3COO)_{16}(H_2O)_4].2CH_3COOH.4H_2O$. *J. Am. Chem. Soc.* **113**, 5873–5874 (1991).

17. Sessoli, R. *et al.* High-spin molecules: $[Mn_{12}O_{12}(O_2CR)_{16}(H_2O)_4]$. *J. Am. Chem. Soc.* **115**, 1804–1816 (1993).

18. Parois, P. *et al.* Pressure-induced Jahn–Teller switching in a Mn_{12} nanomagnet. *Chem. Commun.* **46**, 1881 (2010).

19. Kaszub, W. *et al.* Ultrafast Photoswitching in a Copper-Nitroxide-Based Molecular Magnet. *Angew. Chemie Int. Ed.* **53**, 10636–10640 (2014).

20. Inglis, R. *et al.* Twisting, bending, stretching: strategies for making ferromagnetic $[Mn^{III}_3]$ triangles. *Dalt. Trans.* 9157 (2009) doi:10.1039/b911820a.

21. Bradley, J. M. *et al.* MCD spectroscopy of hexanuclear Mn(III) salicylaldoxime single-molecule magnets. *Dalton Trans.* **39**, 9904–9911 (2010).

22. Carlotto, S. *et al.* The electronic properties of three popular high spin complexes $[TM(acac)_3$, TM = Cr, Mn, and Fe] revisited: an experimental and theoretical study. *Phys. Chem. Chem. Phys.* **19**, 24840–24854 (2017).

23. Davis, T. S., Fackler, J. P. & Weeks, M. J. Spectra of Manganese(III) Complexes. The Origin of the Low-Energy Band. *Inorg. Chem.* **7**, 1994–2002 (1968).

24. Krzystek, J. *et al.* High-frequency and -field EPR spectroscopy of tris(2,4-pentanedionato)manganese(III): investigation of solid-state versus solution Jahn-Teller effects. *Inorg. Chem.* **42**, 4610–8 (2003).

25. Snellenburg, J. J., Laptenok, S. P., Seger, R., Mullen, K. M. & Stokkum, I. H. M. van. Glotaran : A Java -Based Graphical User Interface for the R Package TIMP. *J. Stat. Softw.* **49**, 1–22 (2012).

26. Maçôas, E. M. S., Kananavicius, R., Myllyperkiö, P., Pettersson, M. & Kunttu, H. Ultrafast Electronic and Vibrational Energy Relaxation of Fe(acetylacetonate)$_3$ in Solution. *J. Phys. Chem. A* **111**, 2054–2061 (2007).

27. Beaud, P. *et al.* Ultrafast Structural Phase Transition Driven by Photoinduced Melting of Charge and Orbital Order. *Phys. Rev. Lett.* **103**, 155702 (2009).

28. Yeh, A. T., Shank, C. V & McCusker, J. K. Dynamics Following Photo-Induced Charge Transfer. *Science* **289**, 935–938 (2000).

29. Wallin, S., Davidsson, J., Modin, J. & Hammarström, L. Femtosecond Transient Absorption Anisotropy Study on $[Ru(bpy)_3]^{2+}$ and $[Ru(bpy)(py)_4]^{2+}$ Ultrafast Interligand Randomization of the MLCT State. *J. Phys. Chem. A* **109**, 4697–4704 (2005).

30. Milios, C. J. *et al.* A record anisotropy barrier for a single-molecule magnet. *J. Am. Chem. Soc.* **129**, 2754–2755 (2007).

31. Scholes, G. D. *et al.* Using coherence to enhance function in chemical and biophysical systems. *Nature* **543**, 647–656 (2017).

32. Cho, S. *et al.* Coherence in Metal−Metal-to-Ligand-Charge-Transfer Excited States of a Dimetallic Complex Investigated by Ultrafast Transient Absorption Anisotropy. *J. Phys. Chem. A* **115**, 3990–3996 (2011).

33. Iwamura, M., Takeuchi, S. & Tahara, T. Ultrafast Excited-State Dynamics of Copper(I) Complexes. *Acc. Chem. Res.* **48**, 782–791 (2015).

34. North, J., van de Burgt, L. . & Dalal, N. . A Raman study of the single molecule magnet Mn_{12}-acetate and analogs. *Solid State Commun.* **123**, 75–79 (2002).

35. Rivière, E. *et al.* Magneto-optical control of a Mn_{12} nano-magnet. *J. Mater. Chem.* **20**, 7165–7168 (2010).

36. Milios, C. J. *et al.* Toward a Magnetostructural Correlation for a Family of Mn_6 SMMs. *J. Am. Chem. Soc.* **129**, 12505–12511 (2007).

37. Megerle, U., Pugliesi, I., Schriever, C., Sailer, C. F. & Riedle, E. Sub-50 fs broadband absorption spectroscopy with tunable excitation: putting the analysis of ultrafast molecular dynamics on solid ground. *Appl. Phys. B Lasers Opt.* **96**, 215–231 (2009).

Figures

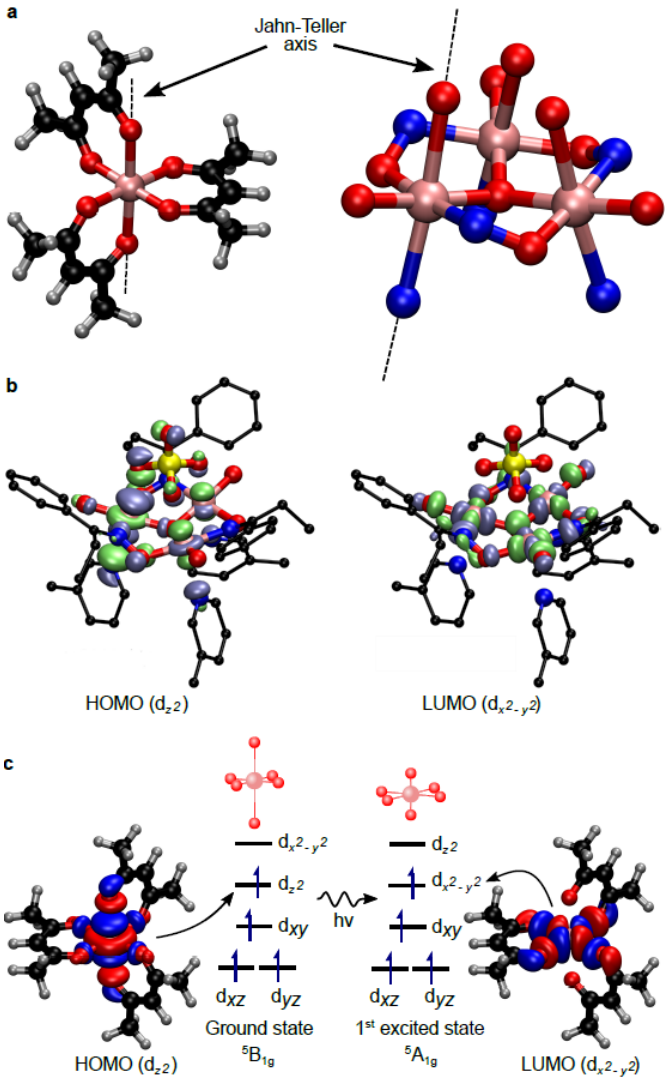

Figure 1 | Structure of Jahn-Teller distorted Mn(III) complexes. ***a*** *$Mn(acac)_3$ and the core of the Mn_3 triangle, showing the axial Jahn-Teller (JT) distortion along the z-axis (perpendicular to the triangle in Mn_3). Colour code: Manganese, purple; oxygen, red; nitrogen, blue; carbon, black; hydrogen, white.* ***b*** *Molecular orbitals (MOs) of Mn_3 obtained using DFT computations at the Def2-SVP level (SI). The highest-occupied MO (HOMO), and other MOs at the same energy, are made up from superpositions of atomic d_{z^2} orbitals, which leads to a JT distortion along the axis perpendicular to the triangle due to the antibonding nature of the d_{z^2} orbital. The lowest-unoccupied MO (LUMO), is comprised of atomic $d_{x^2-y^2}$ orbitals. The hydrogens have been removed from the structure for clarity. Colour code: chloride, yellow.* ***c*** *In $Mn(acac)_3$,*

*the doubly degenerate e_g orbitals (d_{z^2} and $d_{x^2-y^2}$) are directed along the bond axes. However, the single-electron population of the e_g orbitals leads to a lowering of the symmetry and a splitting of the e_g orbitals via the JT distortion. The HOMO of $Mn(acac)_3$ contains the antibonding d_{z^2} orbital. Upon photoexcitation, an electron is promoted to the $d_{x^2-y^2}$ orbital, which destabilises the equatorial bonds and stabilises the axial bonds. The Mn – O bonds along the z-axis are removed for clarity in both **b** and **c**.*

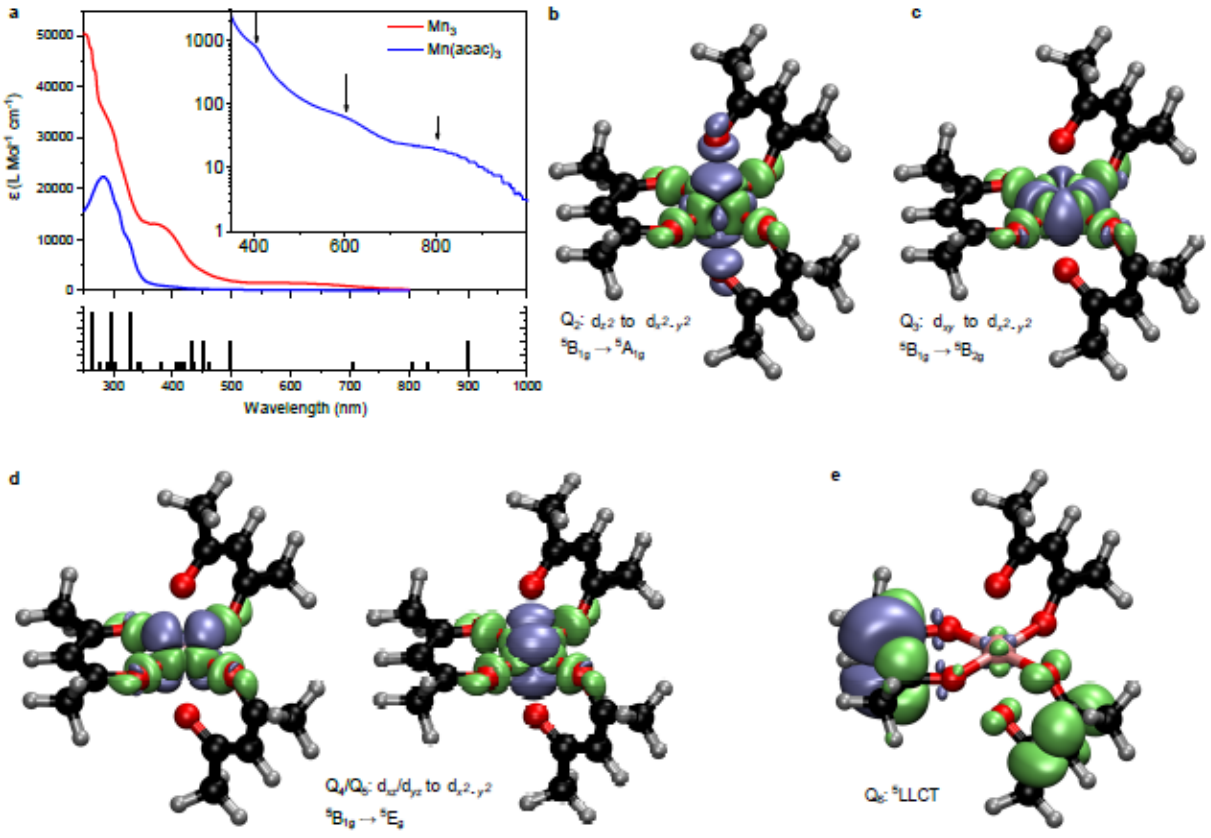

Figure 2 | Electronic absorption spectra of $Mn(acac)_3$ and Mn_3. ***a*** *Electronic absorption spectra of $Mn(acac)_3$ and Mn_3 in ethanol at room temperature. The inset shows the logarithm of the extinction coefficients for $Mn(acac)_3$ to highlight the metal-centred transitions at 800 ($^5B_{1g} \rightarrow {}^5A_{1g}$; Q_2), 600 ($^5B_{1g} \rightarrow {}^5B_{2g}$; Q_3) and 400 ($^5B_{1g} \rightarrow {}^5E_g$; $Q_{4,5}$) nm. The onset of the ligand-to-ligand charge-transfer state (^{5}LLCT; Q_6) can be seen below 400 nm. The bar diagram shows the wavelengths of the calculated transitions (SI), where the bar height is scaled as 1:4:8 for transitions that are spin-forbidden, spin-allowed metal-centred (^{5}MC), and spin-allowed ligand-to-ligand charge-transfer (LLCT), respectively. Difference of electronic density*

between each excited state and the ground state for the five lowest quintet transitions calculated at the CASSCF//NEVPT2 level (SI) are shown in ***b*** *for* $^5B_{1g} \rightarrow {}^5A_{1g}$ *(*Q_2*),* ***c*** *for* $^5B_{1g} \rightarrow {}^5B_{2g}$ *(*Q_3*),* ***d*** *for* $^5B_{1g} \rightarrow {}^5E_g$ *(*$Q_{4,5}$*), and* ***E*** *for* ^{5}*LLCT (*Q_6*). In grey: decrease of electronic density. In green: increase. We note that we do not observe any* ^{5}*LMCT states in the calculations. The Mn – O bond along the z-axis is removed for clarity.*

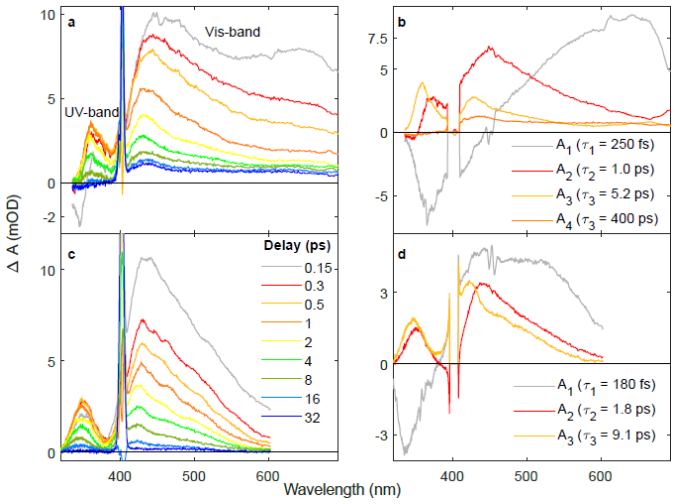

Figure 3 | Ultrafast transient absorption spectra of Mn(acac)$_3$ and Mn$_3$. ***a*** *Difference spectra ΔA at the magic angle for selected time delays from the TA data in ethanol after pumping at 400 nm are shown in* ***a*** *for Mn(acac)*$_3$*. The sharp features around 400 nm are due to scattered pump light. Decay associated spectra (DAS) obtained after a global fit using a sequential fit model are shown in* ***b*** *for Mn(acac)*$_3$*. The pre-exponential factors* A_x *and their corresponding time constants are shown in the legend. The corresponding data for Mn*$_3$ *are shown in* ***c*** *–* ***d.***

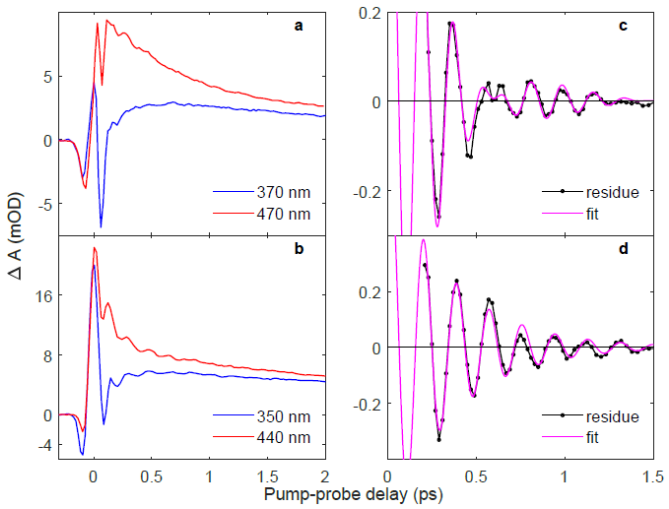

Figure 4 | Kinetic traces of $Mn(acac)_3$ and Mn_3. *Kinetic traces for the UV and Vis bands for* ***a*** *$Mn(acac)_3$ and* ***b*** *Mn_3. The solvent cross-phase modulation can be observed around time-zero. The average of the residues of the global analysis from the data in* ***a*** *and* ***b*** *are shown in* ***C*** *from 426 – 492 nm for the $Mn(acac)_3$ Vis band and* ***D*** *from 435 − 460 nm for the Mn_3 Vis-band. An average over a finite bandwidth was used to enable the observation of the oscillations for longer time delays, which improved the frequency analysis of the oscillations. The signals have been fitted with a sum of n damped cosine-functions* $y(t) = e^{-t/\tau_{osc}} \sum_n B_n cos(2\pi(t - t_c)/T_n)$*, where B_n is the amplitude, τ_{osc} is the dephasing time, which for simplicity was set the same for all frequencies. A phase constant t_c was also fitted but found to be close to zero (cosine-like oscillations). T_n is the period of the n'th frequency. Two frequencies were found at 170 ± 5 and 208 ± 6 cm^{-1} for the $Mn(acac)_3$ Vis-band and one frequency at 181 ± 3 cm^{-1} for the Mn_3 Vis-band. The exponential damping time constants were 325 ± 11 fs for $Mn(acac)_3$ and 360 ± 15 fs for Mn_3.*

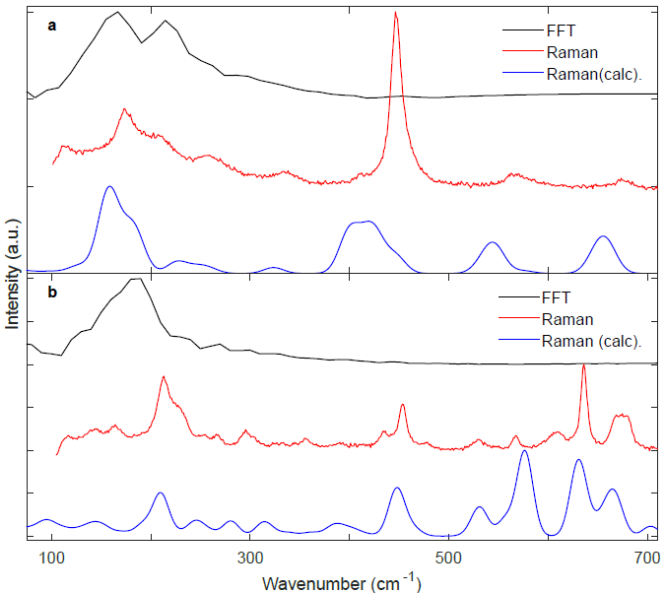

Figure 5 | Analysis of vibrational wavepacket. ***a*** *Fast Fourier transformation of the average residues of the exponential fit for the* $Mn(acac)_3$ *Vis band from the data in Figure 4* ***c****. We found wavenumbers of 167 and 215* cm^{-1}*. Also shown are Raman spectra for* $Mn(acac)_3$ *obtained from exciting crystal grains at 785 nm and the calculated Raman spectrum obtained using DFT at the Def2-SVP level (SI). The calculated modes at 156, 159 and 187* cm^{-1} *involve symmetric stretch motion along all axes but also ligand torsional scissor modes, which implies a complicated reaction coordinate. The corresponding data for* Mn_3 *is shown in* ***b****, where the peak in the Fourier spectrum is centred at 185* cm^{-1} *for the* Mn_3 *Vis-band and the calculations have been obtained at the same level as in* ***a****.*

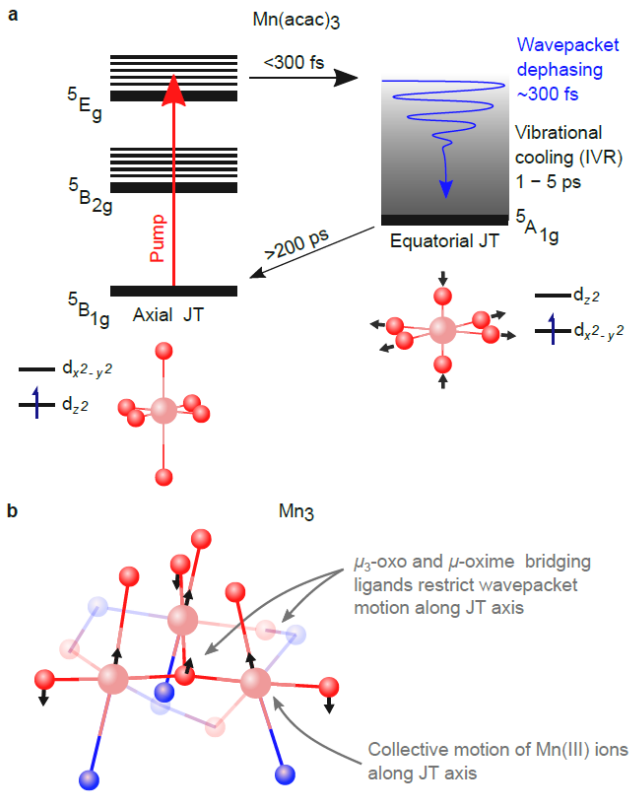

Figure 6 | Photophysical model of the Mn(acac)$_3$ dynamics and wavepacket motion in Mn$_3$. ***a*** *After exciting with 400nm, 120 fs laser pulses into the ^5E_g band in Mn(acac)$_3$, a fast decay via internal conversion (IC) takes place into the $^5A_{1g}$ state, which leads to a switch from axial to equatorial Jahn-Teller distortion (JT) via the formation of a vibrational wavepacket. The wavepacket dephases on a time scale of around 325 fs due to IC, vibrational cooling and intramolecular vibrational redistribution (IVR). The vibrational cooling takes place in 1-5 ps. The lifetime of the $^5A_{1g}$ state in Mn(acac)$_3$ is longer than 200 ps.* ***b*** *Illustration of the vibrational mode of the wave packet in Mn$_3$. The main movement is a collective in-phase oscillation of the bond lengths along the JT axis for all three Mn ions, where the equatorial ligands bond lengths adjust accordingly. When the bond length of the JT axis nitrogen is stretched (JT oxygen bond length is shortening), the equatorial ligands also stretch, and vice versa. The atomic displacements are shown in Supplementary Video 1.*